MDC-2 Benchmarking

J.W. Berkery,[1] Y.Q. Liu,[2] R. Betti,[3] I.T. Chapman,[2] J.P. Graves,[4] J. Manickam,[3] S.A. Sabbagh,[1] Z.R. Wang,[5] L.J. Zheng,[6] and Others...

[1)] *Department of Applied Physics and Applied Mathematics, Columbia University, New York, New York 10027*

[2)] *Euratom/CCFE Fusion Association, Culham Science Centre, Abingdon, OX14 3DB, UK*

[3)] *Princeton Plasma Physics Laboratory, Princeton University, Princeton, New Jersey 08543*

[4)] *École Polytechnique Fédérale de Lausanne (EPFL), Centre de Recherches en Physique des Plasmas, Association EURATOM-Confédération Suisse, 1015 Lausanne, Switzerland*

[5)] *Consorzio RFX, Associazione EURATOM-ENEA sulla Fusione Corso Stati Uniti 4, 35127 Padova, Italy*

[6)] *Institute for Fusion Studies, University of Texas at Austin, Austin, Texas 78712*

(Dated: 19 January 2012)

Abstract

I. INTRODUCTION

Introduction?

II. CODES

A. AEGIS

AEGIS

B. HAGIS

MISHKA
HAGIS

C. MARS-K

MARS-K

D. MISK

PEST[1]
MISK[2] (used in:[3–10]).

III. EQUILIBRIA

A. Solov'ev Equilibrium

The Solov'ev equilibrium is an analytical equilibrium solution to the Grad-Shafranov equation[11,12]. In MARS-K, the Solov'ev equilibrium is written[13]:

$$F(\psi) = 1. \tag{1}$$

$$\frac{\mu_0}{B_0^2} P(\psi) = -\frac{1+\kappa^2}{\kappa R_0^3 q_0}\psi. \tag{2}$$

$$\psi = \frac{\kappa}{2R_0^3 q_0}\left[\frac{R^2 Z^2}{\kappa^2} + \frac{1}{4}\left(R^2 - R_0^2\right)^2 - \epsilon_a^2 R_0^4\right]. \tag{3}$$

This ψ ranges from a negative value at the axis ($-\psi_0$) to zero at the edge. A normalized flux can be written $\psi_n = \psi/\psi_0 + 1$, which goes from 0 on axis to 1 at the edge. Three quantities must be specified: κ, q_0, and $\epsilon_a = a/R_0$. The plasma boundary is specified by:

$$R = R_0\left(1 + 2\epsilon_a \cos\theta\right)^{\frac{1}{2}}, \tag{4}$$

$$Z = \frac{R_0 \epsilon_a \kappa \sin\theta}{\left(1 + 2\epsilon_a \cos\theta\right)^{\frac{1}{2}}}. \tag{5}$$

MISK uses the PEST code[1] to provide the eigenfunction and fluid δW terms. The Solov'ev equilibrium can be explicitly input into PEST, and it is written:

$$F(\Psi) = 1. \tag{6}$$

$$\frac{\mu_0}{B_0^2} P(\Psi) = p_0 - \frac{\Psi}{2\pi}\sqrt{\frac{2c_1 p_0 (1+c_3^2)}{\Psi_{lim}}}. \tag{7}$$

$$\Psi = c_1\left[Z^2\left(R^2 - c_2\right) + \frac{c_3^2}{4}\left(R^2 - R_0^2\right)^2\right]. \tag{8}$$

Here the PEST Ψ goes from 0 at the axis to a positive value, Ψ_{lim}, at the edge, and is related to the MARS ψ by:

$$\psi = \left(\Psi - \Psi_{lim}\right)/2\pi. \tag{9}$$

The two methods are exactly equivalent when:

$$c_1 = \frac{1}{2\kappa R_0^3 q_0} 2\pi \tag{10}$$

$$c_2 = 0 \tag{11}$$

$$c_3 = \kappa \tag{12}$$

$$\Psi_{lim} = \frac{\epsilon_a^2 R_0 \kappa}{2q_0} 2\pi \tag{13}$$

$$p_0 = \frac{1+\kappa^2}{2}\frac{\epsilon_a^2}{R_0^2 q_0^2} \tag{14}$$

$$\alpha_p = \sqrt{\frac{2c_1 p_0 (1+c_3^2)}{\Psi_{\rm lim}}} = \frac{1+\kappa^2}{\kappa q_0 R_0^3}. \tag{15}$$

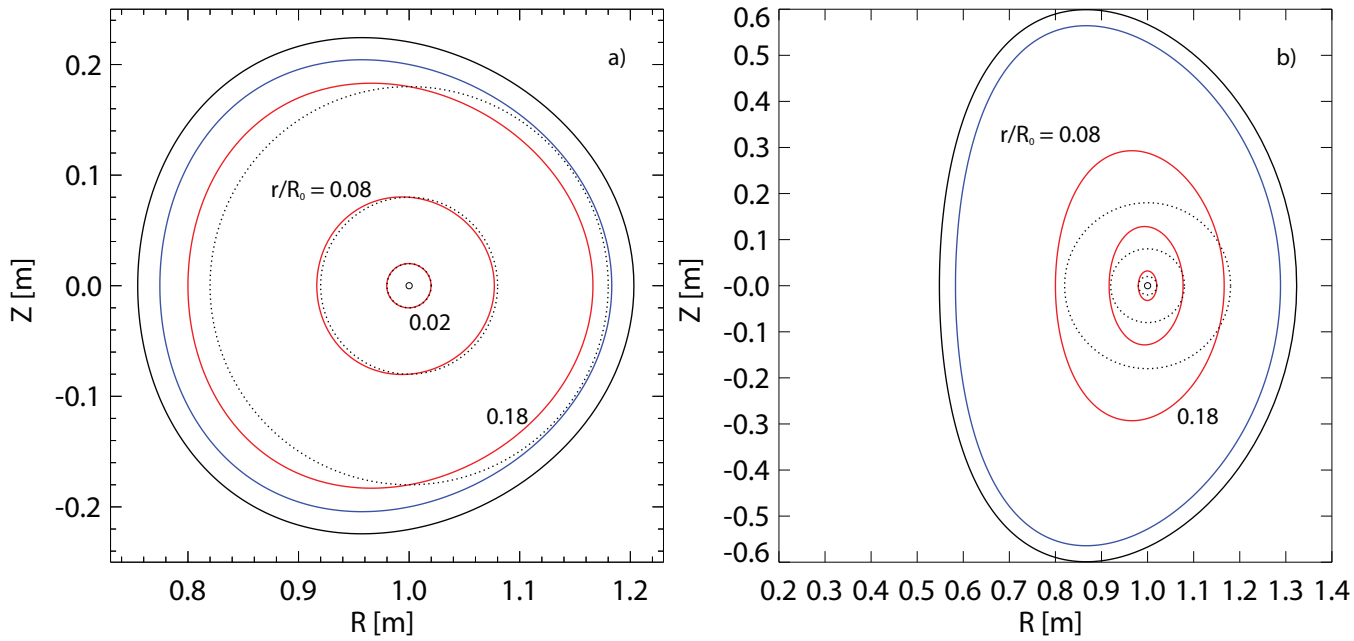

FIG. 1. a) The Solov'ev 1 equilibrium and b) the Solov'ev 3 equilibrium, showing flux surfaces at the edge (blue) and $r/R_0 = 0.02$, 0.08, and 0.18 (red). These last three are compared to their equivalent circles (dashed). Finally, conformal walls having $r_w/a = 1.15$ for Solov'ev 1 and $r_w/a = 1.10$ for Solov'ev 3 are shown in black (see section VIII).

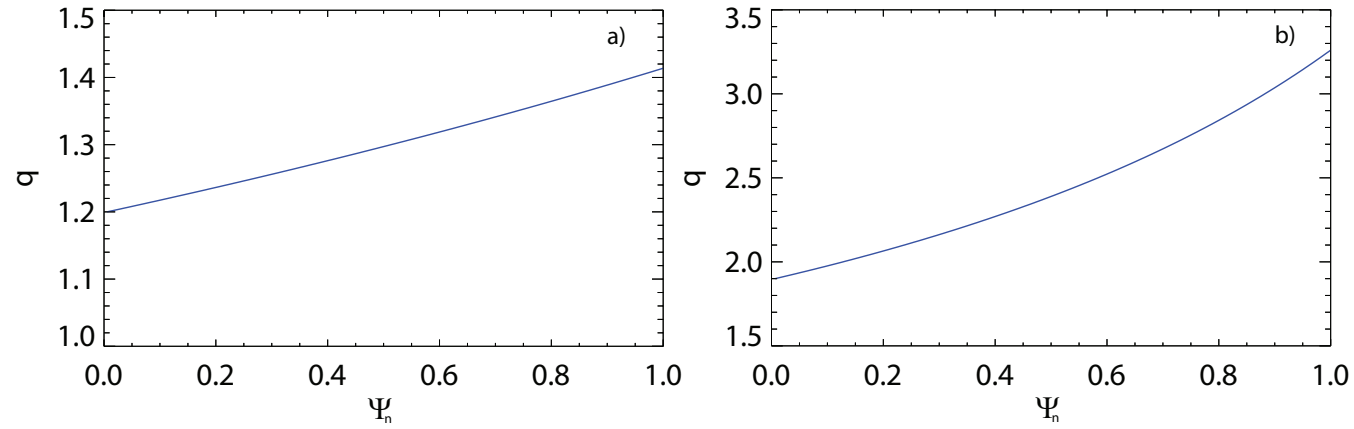

FIG. 2. a) The Solov'ev 1 equilibrium and b) Solov'ev 3 equilibrium q profiles.

To use the analytical Solov'ev equilibrium in `PEST`, one sets `&glotcl lanal=.true.`, in both `mapin` and `modin`. Then one specifies the above quantities in `mapin` where c_1, c_2, and c_3 are listed under `&kerdat` as `c1`, `c2`, and `c3`, p_0 is listed under `&prof` as `p0`, Ψ_{lim} is listed under `&magax` as `psilim`, and R_0 is listed under `&size` as `r`. Also, α_p must be set in `modin` under `&cprofl` as `alphap`.

1. Solov'ev 1

The equilibrium designated "Solov'ev 1" was used in Ref. [13], and is near-circular (Fig. 1a), with no rational surfaces (Fig. 2a). It is specified by the parameters $\kappa = 1$, $q_0 = 1.2$, and $\epsilon_a = 0.2$, and has a $q_{\rm edge} = 1.41371$.

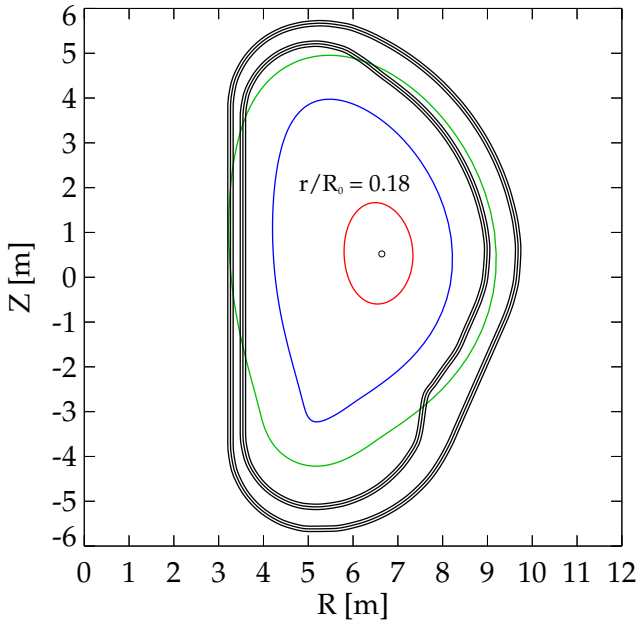

FIG. 3. The ITER equilibrium, showing a flux surface at the edge (blue) and $r/R_0 = 0.18$ (red). Also shown are the ITER double wall (black), and a conformal wall with $r_w/a = 1.5$ (green).

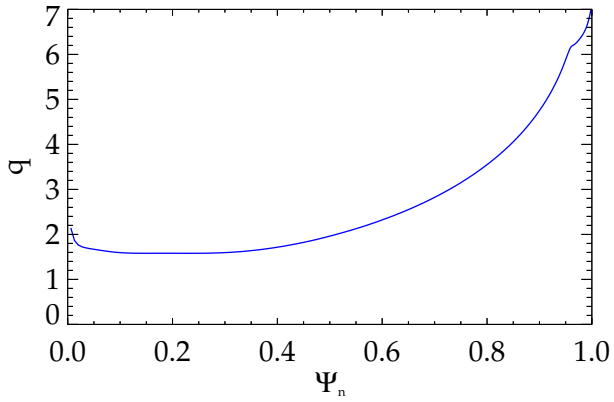

FIG. 4. The ITER equilibrium q profile.

2. Solov'ev 3

The equilibrium designated "Solov'ev 3" was also used in Ref. [13]. This equilibrium is shaped (Fig. 1b), and contains the $q = 2$ and 3 rational surfaces within the plasma (Fig. 2b). It is specified by the parameters $\kappa = 1.6$, $q_0 = 1.9$, and $\epsilon_a = 0.33$, and has a $q_{\rm edge} = 3.263$.

B. ITER

The ITER equilibrium used is the same as is used in WG-7, using the current design of the ITER target for 9 MA operation[14], with $\beta_N = 2.9$. It has $R_0 = 6.2$ m, $B_0 = 5.3$ T, the shape shown in Fig. 3 and the q profile shown in Fig. 4.

IV. FREQUENCY COMPARISONS

A. Density, Temperature, Pressure, and Rotation Frequency Profiles

We will assume for the Solov'ev cases that there are no energetic particles, only thermal ions and electrons, and that $n_e = n_i$ and $T_e = T_i$. Also, for the purposes of determining P from Eqs. 2 or 7, we now set $R_0 = 1$m and $B_0 = 1$T. Then the pressure has the form $P = P_0(1 - \psi_n)$, with $P_0 = 2.210 \times 10^4$ Pa for Solov'ev 1, and $P_0 = 4.273 \times 10^4$ Pa for Solov'ev 3.

Finally we must specify the density profile $n(\Psi)$. For the Solov'ev cases, we use $n = n_0(1-0.7\Psi_n)$. Then the density on axis, n_0, is determined by specifying $(\omega_{ci}/\omega_A)_0$, where $\omega_{A0} = B_0/(R_0\sqrt{\mu_0 m_i n_{i0}})$ and $\omega_{ci0} = eB_0/m_i = 47.906$ MHz. For the comparisons here, we will use $(\omega_{ci}/\omega_A)_0 = 121$, to be consistent with Ref. [13], even though this results in the values of $\omega_{A0} = 395.914$ kHz and the unrealistically high density $n_0 = 1.518 \times 10^{21}$ m^{-3}.

The temperature profile is then determined from $T = P/(2n)$. For the Solov'ev cases this means $T = (P_0/2n_0)(1 - \Psi_n)/(1 - 0.7\Psi_n)$.

For the Solov'ev cases we will use the $E \times B$ frequency profile $\omega_E = \omega_{E0}\,(1 - \Psi_n)$, and a range of constant values of ω_{E0}. For the moment, we will assume $\omega_E/\omega_{A0} = 1 \times 10^{-2}$ or $\omega_{E0} = 3.959$ kHz as a nominal value. The toroidal rotation frequency can then be found by a radial force balance so that $\omega_{\rm rot} = \omega_E + \omega^i_{*N} + \omega^i_{*T}$, where ω^i_{*N} and ω^i_{*T} are defined in the next subsection.

For the ITER case instead of using analytically prescribed functions for the pressure, density, temperature, and rotation, we will use profiles determined for the WG7 ITER equilibrium. Additionally, the ITER case will have three separate species, each with their own pressure: ions, electrons, and alpha particles. The following are given, as profiles of Ψ: $n_\alpha/(n_e + n_i)$, n_e, T_e, T_i, $P_\alpha/(P_e + P_i)$, and $\omega_{\rm rot}$. The ion density is taken to be equal to the electron density, ie. quasineutrality is not enforced. The ion and electron pressures are determined from $P_e = n_e T_e$, and $P_i = n_i T_i$, which then determines P_α as well.

Figure 5 shows the profiles of density, pressure, and temperature, normalized to the axis values, which are given in Table I. Figure 5 also shows profiles of rotation and the diamagnetic frequencies, ω_{*N} and ω_{*T}. These are also normalized to the axis values, found in Table II, along with the consistent ω_{E0} values.

B. Diamagnetic Frequencies

The density and temperature gradient components of the diamagnetic frequency are defined in SI units (Hz):

$$\omega^j_{*N} = -\frac{T_j}{2\pi Z_j e n_j}\frac{dn_j}{d\Psi}, \tag{16}$$

$$\omega^j_{*T} = -\frac{1}{2\pi Z_j e}\frac{dT_j}{d\Psi}. \tag{17}$$

For the Solov'ev equilibria these can be written analytically as:

$$\omega^i_{*N} = -\omega^e_{*N} = \frac{0.7T_0/e}{2\pi\Psi_a}\left(\frac{1-\Psi_n}{(1-0.7\Psi_n)^2}\right), \tag{18}$$

$$\omega^i_{*T} = -\omega^e_{*T} = \frac{0.3T_0/e}{2\pi\Psi_a}\left(\frac{1}{(1-0.7\Psi_n)^2}\right), \tag{19}$$

where $\Psi_a = -\psi_0 = \Psi_{\rm lim}/2\pi$ from Eq. 13.

C. Collision Frequency

Although in general collisionality can impact kinetic stability calculations, and there are various ways of expressing collisionality[7], for the comparisons here, all collision frequencies are taken to be zero.

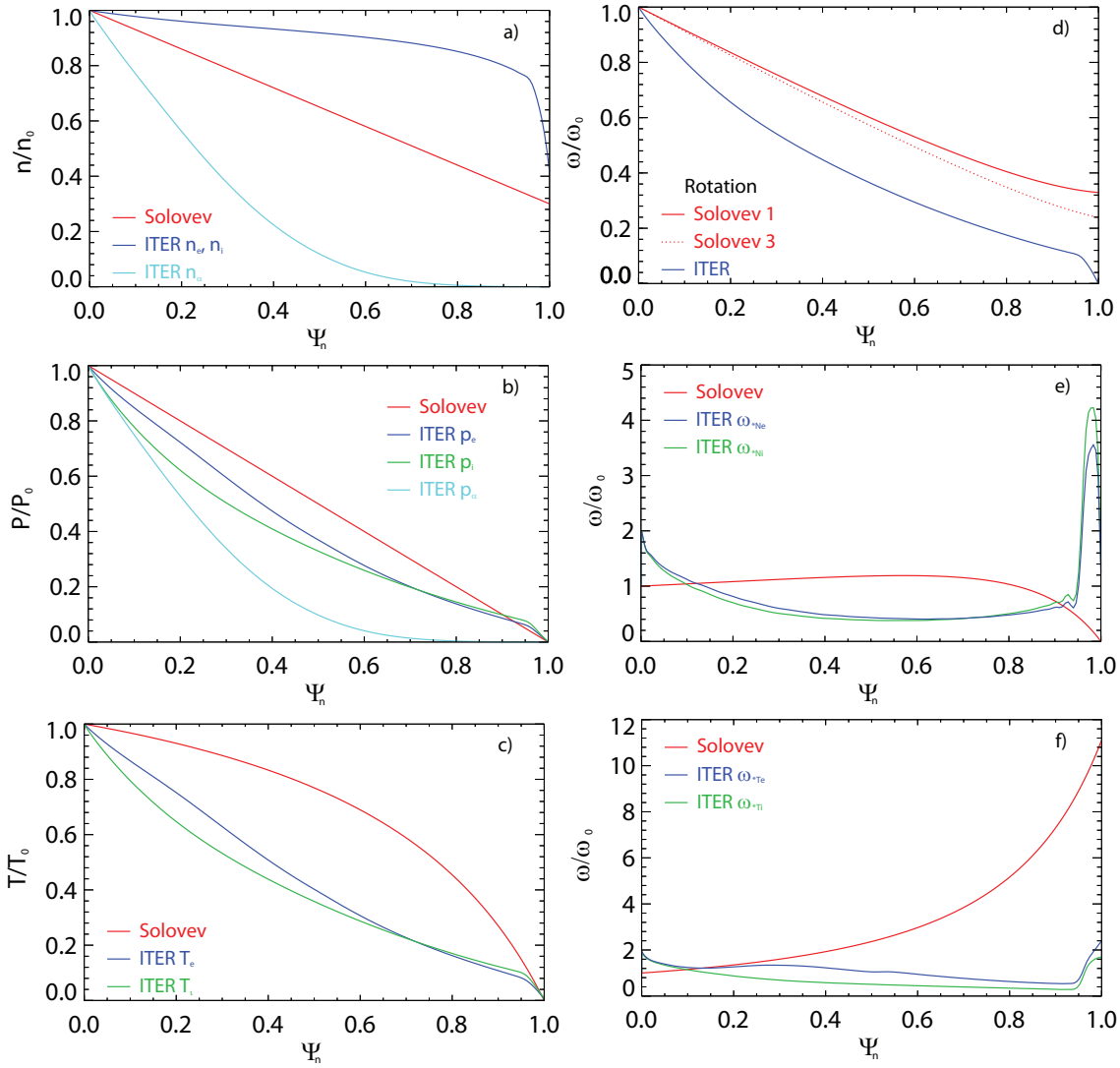

FIG. 5. Normalized profiles of a) density, b) pressure, c) temperature, d) rotation, e) ω_{*N}, and f) ω_{*T}.

	$n_{i0}[10^{19}\mathrm{m}^{-3}]$	$n_{i0}[10^{19}\mathrm{m}^{-3}]$	$n_{\alpha 0}[10^{19}\mathrm{m}^{-3}]$	p_{i0} [kPa]	p_{e0} [kPa]	$p_{\alpha 0}$ [kPa]	T_{i0} [keV]	T_{e0} [keV]
Solov'ev 1	151.795		0	11.052		0	0.045	
Solov'ev 3				21.365			0.088	
ITER	7.220		0.167	362.306	396.200	156.739	31.320	34.250

TABLE I. Density, pressure, and temperature values on axis for each of the cases.

	$\omega_{\mathrm{rot}0}$ [kHz]	ω_{E0} [kHz]	ω_{*Ne0} [kHz]	ω_{*Ni0} [kHz]	ω_{*Te0} [kHz]	ω_{*Ti0} [kHz]
Solov'ev 1	4.393	3.959*	0.304		0.130	
Solov'ev 3	4.264		0.213		0.091	
ITER	6.032*	3.998	-0.154	0.140	-0.960	1.805

TABLE II. Rotation frequency, ω_E, ω_{*N}, and ω_{*T} values on axis for each of the cases. *nominal values.

D. Bounce Frequency

Figure 6a shows the normalized, dimensionless ion bounce frequencies calculated by `MISK` and `MARS-K` compared to the large aspect ratio approximation, using the Solov'ev 1 equilibrium at the $\epsilon_r = 0.08$, $\psi_n = 0.160$ surface vs. Λ. Figure 7a shows the normalized ion bounce frequencies calculated by `MISK` and `MARS-K` compared to the large aspect ratio approximation, using the Solov'ev 3 equilibrium at the $\epsilon_r = 0.33$, $\psi_n = 1$ surface (the plasma boundary) vs. Λ.

Figure 8a shows the normalized ion bounce frequencies calculated by `MISK` and `MARS-K`, using the ITER equilibrium at the $\epsilon_r = 0.322$, $\psi_n = 0.982$ surface (very close to the plasma boundary) vs. Λ.

Figure 9a shows the normalized ion bounce frequencies calculated by `MISK` and `MARS-K` at maximum Λ compared to the deeply trapped particle limit, using the Solov'ev 1 equilibrium and the Solov'ev 3 equilibrium vs. ϵ_r.

1. Large Aspect Ratio Formula

In the large aspect ratio limit, the particle bounce frequency can be written[15,16]:

$$\frac{\omega_b}{\sqrt{2\varepsilon/m_i}} = \frac{\sqrt{2\epsilon_r\Lambda}}{4qR_0}\frac{\pi}{K(k)} \quad \text{(trapped)}, \tag{20}$$

$$\frac{\omega_b}{\sqrt{2\varepsilon/m_i}} = \frac{\sqrt{1-\Lambda+\epsilon_r\Lambda}}{2qR_0}\frac{\pi}{K(1/k)} \quad \text{(circulating)}. \tag{21}$$

where $\Lambda = \mu B_0/\varepsilon$, $\epsilon_r = r/R_0$ (with $r = R - R_0$), K is the complete elliptic integral of the first kind, and

$$k = \left[\frac{1-\Lambda+\epsilon_r\Lambda}{2\epsilon_r\Lambda}\right]^{\frac{1}{2}}. \tag{22}$$

2. Deeply Trapped Particle Formula

In the limit of deeply trapped particles, one can show that for the Solov'ev equilibrium the bounce frequency can be written:

$$\frac{\omega_b}{\sqrt{2\varepsilon/m_i}} = \frac{1}{q_0}\left(\frac{F^2}{1+2\epsilon_r} + \frac{\kappa^2\epsilon_r^2}{q_0^2}\right)^{-1}\left[\frac{F^2\epsilon_r}{2\left(1+2\epsilon_r\right)} + \frac{\kappa^2\epsilon_r^3}{q_0^2} + \frac{\left(1-\kappa^2\right)\epsilon_r^2}{2q_0^2}\left(1+2\epsilon_r\right)\right]^{\frac{1}{2}} \tag{23}$$

3. General Formula

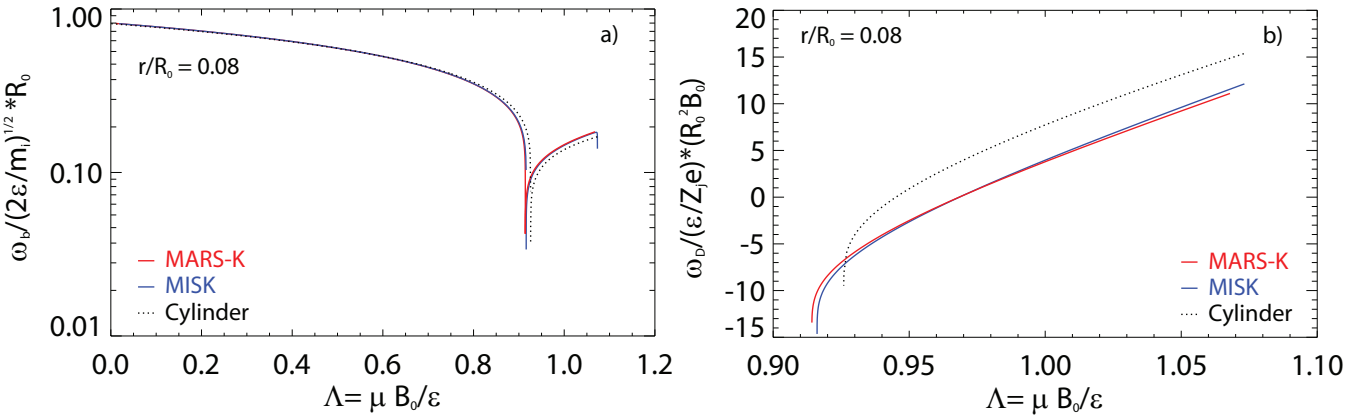

FIG. 6. a) Ion bounce frequency and b) ion precession drift frequency calculated by `MISK` and `MARS-K` compared to the large aspect ratio approximation for the $\epsilon_r = 0.08$ surface of the Solov'ev 1 case, vs. Λ. The left branch of a) is for circulating ions and the right branch is for trapped ions. Plot b) can be directly compared to the same one produced by `MARS-K` in Ref. [13], Fig. 1(b).

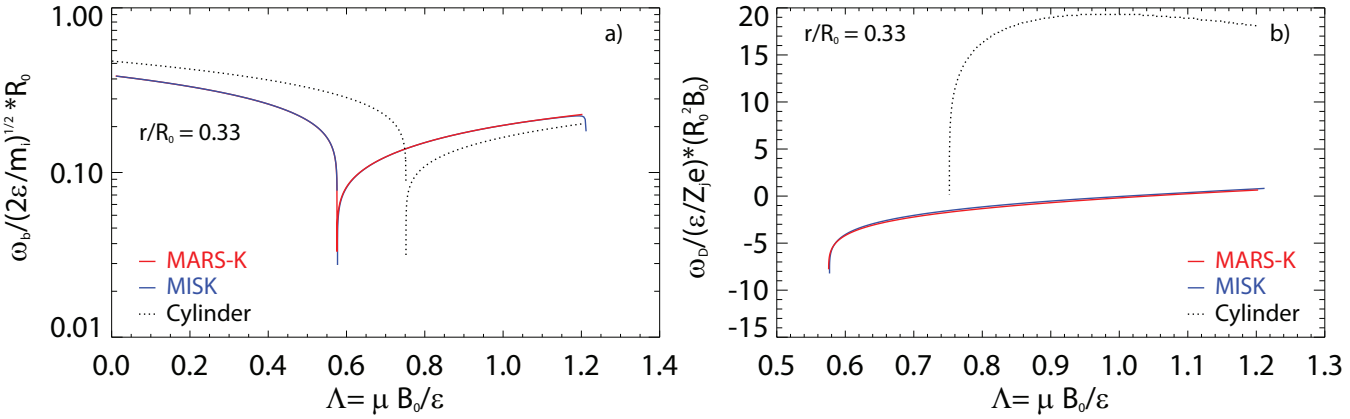

FIG. 7. a) Ion bounce frequency and b) ion precession drift frequency calculated by `MISK` and `MARS-K` compared to the large aspect ratio approximation at the outer surface of the Solov'ev 3 case, vs. Λ. The left branch of a) is for circulating ions and the right branch is for trapped ions.

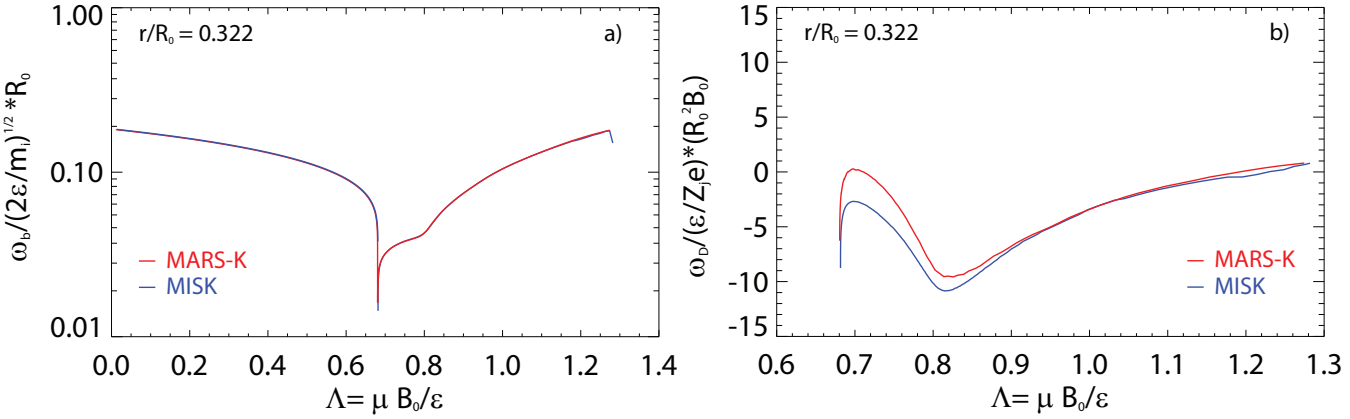

FIG. 8. a) Ion bounce frequency and b) ion precession drift frequency calculated by `MISK` and `MARS-K` at the $\epsilon_r = 0.322$ surface (very close to the outer surface) of the ITER case, vs. Λ. The left branch of a) is for circulating ions and the right branch is for trapped ions.

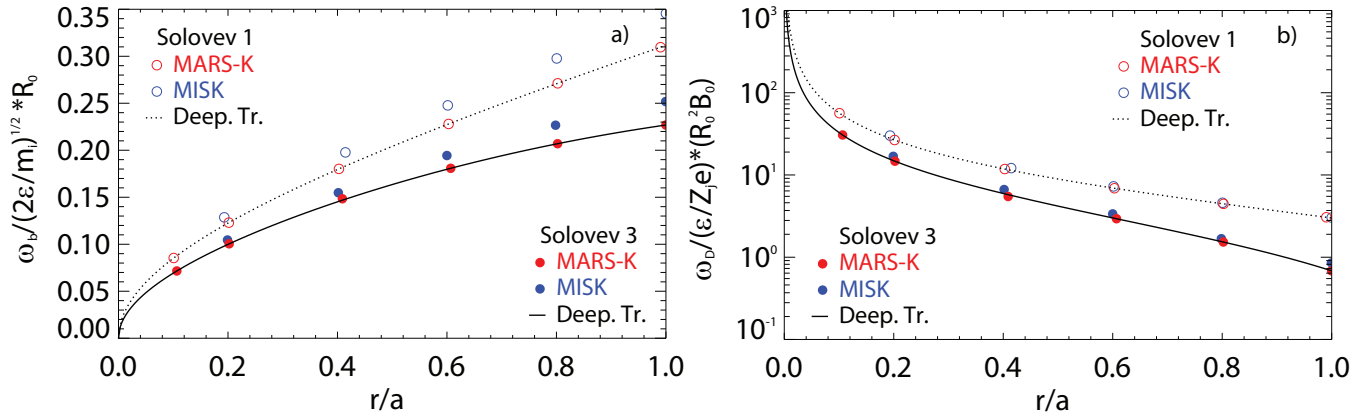

FIG. 9. a) Ion bounce frequency and b) ion precession drift frequency calculated by MISK and MARS-K at maximum Λ compared to the deeply trapped particle limit for the Solov'ev 1 and 3 cases, vs. ϵ_r. Note: this figure is out of date for the MISK results and needs to be remade if used.

E. Magnetic Precession Drift Frequency

Figure 6b shows the normalized ion precession drift frequencies calculated by MISK and MARS-K compared to the large aspect ratio approximation, using the Solov'ev 1 equilibrium at the $\epsilon_r = 0.08$, $\psi_n = 0.160$ surface, vs. Λ. A more sophisticated analytic approach to calculate the precession drift frequency for arbitrarily shaped toroidal plasmas, by doing a higher order expansion of the toroidal equilibrium in terms of toroidicity, elongation, triangularity, etc... was also compared to this case and was quite close to the MARS-K result.

Figure 7b shows the normalized ion precession drift frequencies calculated by MISK and MARS-K compared to the large aspect ratio approximation, using the Solov'ev 3 equilibrium at the $\epsilon_r = 0.33$, $\psi_n = 1$ surface (the plasma boundary), vs. Λ.

Figure 8a shows the normalized ion precession drift frequencies calculated by MISK and MARS-K, using the ITER equilibrium at the $\epsilon_r = 0.322$, $\psi_n = 0.982$ surface (very close to the plasma boundary) vs. Λ.

Figure 9b shows the normalized ion precession drift frequencies calculated by MISK and MARS-K at maximum Λ compared to the deeply trapped particle limit, using the Solov'ev 1 equilibrium and the Solov'ev 3 equilibrium vs. ϵ_r.

1. Large Aspect Ratio Formula

The large aspect ratio precession drift frequency for trapped particles[13,16]:

$$\frac{\omega_D}{\varepsilon/(Z_j e)} = \frac{2q\Lambda}{R_0^2 \epsilon_r B_0}\left[(2s+1)\frac{E(k)}{K(k)} + 2s\left(k^2-1\right) - \frac{1}{2}\right], \tag{24}$$

where $s = (r/q)(dq/dr)$ is the magnetic shear and E is the complete elliptic integral of the second kind.

We can also write this expression in a way that separates it into a "main" term and a "q shear" term:

$$\frac{\omega_D}{\varepsilon/(Z_j e)} = \frac{2q\Lambda}{R_0^2 \epsilon_r B_0}\left[\frac{E(k)}{K(k)} - \frac{1}{2}\right] + \frac{2q\Lambda}{R_0^2 \epsilon_r B_0}\left[2s\left(\frac{E(k)}{K(k)} + k^2 - 1\right)\right]. \tag{25}$$

2. Deeply Trapped Particle Formula

In the limit of deeply trapped particles, one can show that for the Solov'ev equilibrium the precession drift frequency can be written:

$$\frac{\omega_D}{\varepsilon/(Z_j e)} = \frac{q_0}{R_0 \kappa \epsilon_r}\left(\frac{F^2}{1+2\epsilon_r} + \frac{\kappa^2 \epsilon_r^2}{q_0^2}\right)^{-1}\left[\frac{F^2}{(1+2\epsilon_r)^2} - \frac{\kappa^2 \epsilon_r}{q_0^2}\right] \tag{26}$$

3. General Formula

The general formula for the bounce-averaged magnetic precession drift frequency comes from Ref. [17], and is given by:

$$\omega_D = \frac{1}{Z_j e}\frac{\partial J/\partial \Psi}{\partial J/\partial \varepsilon}, \tag{27}$$

where

$$J = \int m_j v_\parallel d\boldsymbol{\ell}, \tag{28}$$

is the equilibrium longitudinal invariant of the particle parallel motion. This equation for ω_D is broken into two parts. Using $\tau = \partial J/\partial \varepsilon$,[17] we have:

$$\omega_D = \frac{\varepsilon}{Z_j e}\frac{1}{\tau}\frac{2}{v^2}\frac{\partial}{\partial \Psi}\left(\int v_\parallel d\boldsymbol{\ell}\right) \tag{29}$$

$$= \frac{\varepsilon}{Z_j e}\frac{1}{\tau}\frac{2}{v^2}\left[\int \frac{\partial v_\parallel}{\partial \Psi} d\boldsymbol{\ell} + \int v_\parallel \frac{\partial d\boldsymbol{\ell}}{\partial \Psi}\right] \tag{30}$$

$$= \frac{\varepsilon}{Z_j e}\frac{1}{\tau}\int \frac{d\boldsymbol{\ell}}{v_\parallel}\left[\frac{1}{v^2}\frac{\partial v_\parallel^2}{\partial \Psi}\right] + \frac{\varepsilon}{Z_j e}\frac{1}{\tau}\int \frac{2v_\parallel}{v^2}\frac{\partial}{\partial \Psi}\left(\frac{d\boldsymbol{\ell}}{d\theta}\right) d\theta \tag{31}$$

Let us now define[17]

$$g = \frac{B_\theta^2}{B}\frac{d\boldsymbol{\ell}}{d\theta}. \tag{32}$$

Then

$$\omega_D = \frac{\varepsilon}{Z_j e}\frac{1}{\tau}\int \frac{d\boldsymbol{\ell}}{v_\parallel}\left[\frac{1}{\varepsilon}\frac{\partial}{\partial \Psi}(\varepsilon - \mu B)\right] + \frac{\varepsilon}{Z_j e}\frac{1}{\tau}\int \frac{2v_\parallel}{v^2}\frac{\partial}{\partial \Psi}\left(\frac{gB}{B_\theta^2}\right) d\theta \tag{33}$$

$$= -\frac{\varepsilon}{Z_j e}\frac{1}{\tau}\int \frac{d\boldsymbol{\ell}}{v_\parallel}\left[\frac{\mu}{\varepsilon}\frac{\partial B}{\partial \Psi}\right] + \frac{\varepsilon}{Z_j e}\frac{1}{\tau}\int \frac{2v_\parallel}{v^2}\frac{gB}{B_\theta^2}\left(\frac{1}{g}\frac{\partial g}{\partial \Psi} + \frac{B_\theta^2}{B}\frac{\partial}{\partial \Psi}\left(\frac{B}{B_\theta^2}\right)\right) d\theta \tag{34}$$

$$= -\frac{\varepsilon}{Z_j e}\frac{1}{\tau}\int \frac{d\boldsymbol{\ell}}{v_\parallel}\left[\frac{\Lambda}{B_0}\frac{\partial B}{\partial \Psi}\right] + \frac{\varepsilon}{Z_j e}\frac{1}{\tau}\int d\boldsymbol{\ell}\frac{2v_\parallel}{v^2}\left[\frac{B_\theta^2}{B}\frac{\partial}{\partial \Psi}\left(\frac{B}{B_\theta^2}\right) - \frac{1}{B_\theta^2}\left(\mu_0\frac{\partial p}{\partial \Psi} + \frac{F}{R^2}\frac{\partial F}{\partial \Psi}\right)\right], \tag{35}$$

where we have used[17]

$$\frac{1}{g}\frac{\partial g}{\partial \Psi} = -\frac{1}{B_\theta^2}\left(\mu_0\frac{\partial p}{\partial \Psi} + \frac{F}{R^2}\frac{\partial F}{\partial \Psi}\right). \tag{36}$$

Equation 35 is the form for ω_D used in `MARS-K`. The first term is called D_μ and the second term is D_B. An equivalent expression is used in `MISK`.

Note that at the turning points $v_\parallel \to 0$ causes a singularity in Eq. 35, but this singularity is integrable.

V. ENERGY INTEGRAL OF THE FREQUENCY RESONANCE FRACTION

A major part of the kinetic calculation is the energy integration of the frequency resonance fraction:

$$I_\varepsilon(\Psi,\Lambda,l)=\int_0^\infty \frac{n\left(\omega_{*N}+\left(\hat{\varepsilon}-\frac{3}{2}\right)\omega_{*T}\right)+n\omega_E-\omega_r-i\gamma}{n\left(\omega_D+(l+\alpha nq)\,\omega_b\right)-i\nu_{\text{eff}}+n\omega_E-\omega_r-i\gamma}\hat{\varepsilon}^{\frac{5}{2}}e^{-\hat{\varepsilon}}d\hat{\varepsilon}. \tag{37}$$

where $\hat{\varepsilon}=\varepsilon/T$, n is the toroidal mode number (not the density), and $\alpha=0$ for trapped particles or $\alpha=1$ for circulating particles. This quantity can be evaluated based only upon the frequencies already described, for both ions and electrons. Nominally, $\nu_{\text{eff}}=0$ as specified in subsection IV C, and we will take $\omega_r=0$ and $\gamma=0$. Note that when collisionality is zero, having a small imaginary component (via γ) in the denominator is beneficial to avoid singularities in the integration[10]. Since we are taking $\nu_{\text{eff}}=0$ and $\gamma=0$, there are poles on the real energy axis, which must be accounted for (see next subsection).

If we choose a particular Ψ surface, then ω_{*N}, ω_{*T}, and ω_E are constants defined by Figs. 5d-f and Table II. The precession drift and bounce frequencies are functions of both Λ and $\hat{\varepsilon}$ still, as indicated in Figs. 6, 7, and 8. Performing the energy integration, we can plot I_ε as a function of Λ. Figure 10 shows each l component of I_ε from -4 to 4 for thermal ions in the Solov'ev 1 equilibrium at $r/R_0=0.08$ ($\Psi_n=0.16$), the same surface chosen in Fig. 6. Figures 11 and 12 show each l component of I_ε from -4 to 4 for thermal ions in the Solov'ev 3 equilibrium at $r/R_0=0.252$ ($\Psi_n=0.585, q=2.5$), and the ITER equilibrium at $r/R_0=0.322$ ($\Psi_n=0.982$, respectively.

A. Analytical Solutions

One major difference between `MISK` and `MARS-K` is that `MISK` performs this integration numerically, whereas `MARS-K` performs it analytically[16]. Analytical solutions are possible only under certain constraints.

1. Kruskal-Oberman Limit

In the Kruskal-Oberman limit[18], $|\omega_E-\omega|\to\infty$ and therefore

$$I_\varepsilon(\Psi,\Lambda,l)\to I_\varepsilon^{KO}=\int_0^\infty \hat{\varepsilon}^{\frac{5}{2}}e^{-\hat{\varepsilon}}d\hat{\varepsilon}=\frac{15\sqrt{\pi}}{8}. \tag{38}$$

In this limit δW_K is purely real, and independent of the mode-particle resonances. This allows a good check on the $|\langle H/\hat{\varepsilon}\rangle|^2$ part of the problem.

2. ν_{eff} = constant (no energy dependence), and $l=0$ for trapped particles

This is the case for trapped particles without energy-dependent collisions, with only the precession drift and no bounce frequency,

$$I_\varepsilon=\int_0^\infty \frac{\Omega_*^a+\Omega_n+\hat{\varepsilon}\Omega_*^b}{\hat{\varepsilon}+\Omega_n}\hat{\varepsilon}^{\frac{5}{2}}e^{-\hat{\varepsilon}}d\hat{\varepsilon}, \tag{39}$$

where $\Omega_n=(n\omega_E-\omega-i\nu_{\text{eff}})/(n\overline{\omega_D})$, $\Omega_*^a=(n\omega_{*N}-\frac{3}{2}n\omega_{*T}+i\nu_{\text{eff}})/(n\overline{\omega_D})$, $\Omega_*^b=\omega_{*T}/\overline{\omega_D}$, and $\omega_D=\overline{\omega_D}\hat{\varepsilon}$ (ie. $\overline{\omega_D}$ is the non-energy dependent portion of ω_D). The solution is given in Ref. [16], Eq. 30:

$$I_\varepsilon=\frac{15\sqrt{\pi}}{8}\Omega_*^b+2\sqrt{\pi}\left(\Omega_n+\Omega_*^a-\Omega_n\Omega_*^b\right)\left[\frac{3}{8}-\frac{1}{4}\Omega_n+\frac{1}{2}\Omega_n^2+i\frac{1}{2}\Omega_n^{\frac{5}{2}}Z\left(i\Omega_n^{\frac{1}{2}}\right)\right], \tag{40}$$

where Z is the plasma dispersion function.

Note that the resonance condition is $\hat{\varepsilon}=-Re(\Omega_n)$. Therefore this solution is valid and there are no poles on the real, positive energy axis as long as $Re(\Omega_n)>0$ or $Im(\Omega_n)\neq 0$, ie. there exists some finite damping, $\gamma+\nu_{\text{eff}}\neq 0$. If

there are poles along the path of integration, then their residues must be calculated. Equation 39 can be written as $\int f(z)dz$, where $z = \hat{\varepsilon}$, and the residue is given by

$$\mathrm{Res}(f, z \to -\Omega_n) = \lim_{z \to -\Omega_n} (z + \Omega_n) f(z) = \left(\Omega_n + \Omega_*^a - \Omega_n \Omega_*^b\right) (-\Omega_n)^{\frac{5}{2}} e^{\Omega_n} \tag{41}$$

Finally, one must also be careful of the locations in (Ψ, Λ) space where there is a drift reversal (ω_D goes through zero). In this case, one can show that the analytical solution to Eq. 37 is:

$$I_\varepsilon = \frac{15\sqrt{\pi}}{8} \left[\frac{n\left(\omega_{*N} + 2\omega_{*T}\right) + n\omega_E - \omega_r - i\gamma}{-i\nu_{\mathrm{eff}} + n\omega_E - \omega_r - i\gamma} \right]. \tag{42}$$

When this analytical solution is used in `MISK`, we use Eq. 42 when $\Omega_n > 1000$ or $\Omega_*^a > 1000$ or $\Omega_*^b > 1000$. How does `MARS-K` deal with it?

3. ν_{eff} = constant (no energy dependence), $l \neq 0$ for trapped particles, and $|\omega_D| \ll |l\omega_b|$

This is the case again without energy-dependent collisions, for trapped particles with $l \neq 0$ where the precession drift frequency is neglected with respect to the bounce frequency. If we now define $\Omega_{n2} = (n\omega_E - \omega - i\nu_{\mathrm{eff}})/(nl\overline{\omega_b})$, $\Omega_*^{a2} = (n\omega_{*N} - \frac{3}{2}n\omega_{*T} + i\nu_{\mathrm{eff}})/(nl\overline{\omega_b})$, $\Omega_*^{b2} = \omega_{*T}/\overline{l\omega_b}$, and $\omega_b = \overline{\omega_b}\hat{\varepsilon}^{\frac{1}{2}}$ (ie. $\overline{\omega_b}$ is the non-energy dependent portion of ω_b), then

$$I_\varepsilon = \int_0^\infty \frac{\Omega_*^{a2} + \Omega_{n2} + \hat{\varepsilon}\Omega_*^{b2}}{\frac{\overline{\omega_D}}{l\overline{\omega_b}}\hat{\varepsilon} + \hat{\varepsilon}^{\frac{1}{2}} + \Omega_{n2}} \hat{\varepsilon}^{\frac{5}{2}} e^{-\hat{\varepsilon}} d\hat{\varepsilon}. \tag{43}$$

With $\overline{\omega_D}/l\overline{\omega_b} \to 0$ this has the analytical solution

$$\begin{aligned} I_\varepsilon = &-\Omega_*^{b2}\left(\frac{15\sqrt{\pi}}{8}\Omega_{n2} - 6\right) + 2\sqrt{\pi}\left(\Omega_{n2} + \Omega_*^{a2} + \Omega_{n2}^2\Omega_*^{b2}\right)\left[-\Omega_{n2}\left(\frac{3}{8} + \frac{1}{4}\Omega_{n2}^2 + \frac{1}{2}\Omega_{n2}^4\right) - \frac{1}{2}\Omega_{n2}^6 Z\left(\Omega_{n2}\right)\right. \\ &\left. + \frac{1}{2\sqrt{\pi}}\left(\Omega_{n2}^4 + \Omega_{n2}^2 + 2\right) + \frac{1}{2\sqrt{\pi}} e^{-\Omega_{n2}^2}\left(i\pi - \mathrm{Ei}(\Omega_{n2}^2) + \frac{1}{2}\ln(\Omega_{n2}^2) - \frac{1}{2}\ln(\Omega_{n2}^{-2}) - 2\ln(\Omega_{n2})\right)\right]. \end{aligned} \tag{44}$$

In this case, Eq. 43 has two residues when $\overline{\omega_D}/l\overline{\omega_b}$ is retained, which are given by:

$$\mathrm{Res}(f, z = z_1) = \frac{2\left(\Omega_{n2} + \Omega_*^{a2} + z_1^2\Omega_*^{b2}\right) z_1^6 e^{-z_1^2}}{(z_1 - z_2)}, \tag{45}$$

$$\mathrm{Res}(f, z = z_2) = \frac{2\left(\Omega_{n2} + \Omega_*^{a2} + z_2^2\Omega_*^{b2}\right) z_2^6 e^{-z_2^2}}{(z_2 - z_1)}, \tag{46}$$

with

$$z_1 = \frac{1}{2}\frac{\overline{\omega_D}}{l\overline{\omega_b}}\left(-1 + \sqrt{1 - 4\frac{l\overline{\omega_b}}{\overline{\omega_D}}\Omega_{n2}}\right) \tag{47}$$

$$z_2 = \frac{1}{2}\frac{\overline{\omega_D}}{l\overline{\omega_b}}\left(-1 - \sqrt{1 - 4\frac{l\overline{\omega_b}}{\overline{\omega_D}}\Omega_{n2}}\right) \tag{48}$$

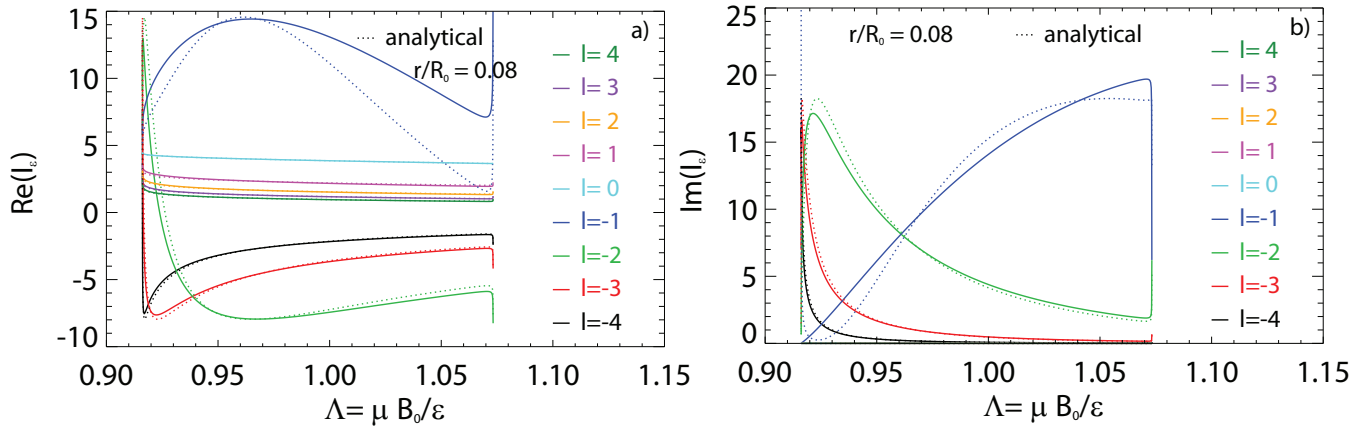

FIG. 10. a) Real and b) imaginary components of I_ε for each l from -4 to 4, vs. Λ for thermal ions in the Solov'ev 1 equilibrium at $r/R_0 = 0.08$ ($\Psi_n = 0.16$), calculated by `MISK`. Solid lines are the usual numerical method, while dashed lines use the analytical methods outlined in subsection V A.

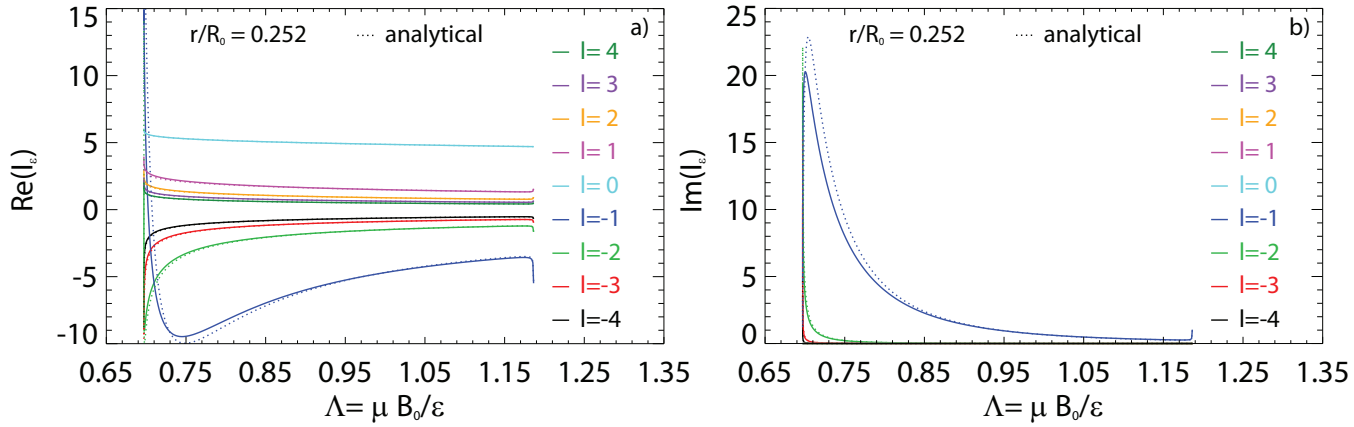

FIG. 11. a) Real and b) imaginary components of I_ε for each l from -4 to 4, vs. Λ for thermal ions in the Solov'ev 3 equilibrium at $r/R_0 = 0.252$ ($\Psi_n = 0.585, q = 2.5$), calculated by `MISK`. Solid lines are the usual numerical method, while dashed lines use the analytical methods outlined in subsection V A.

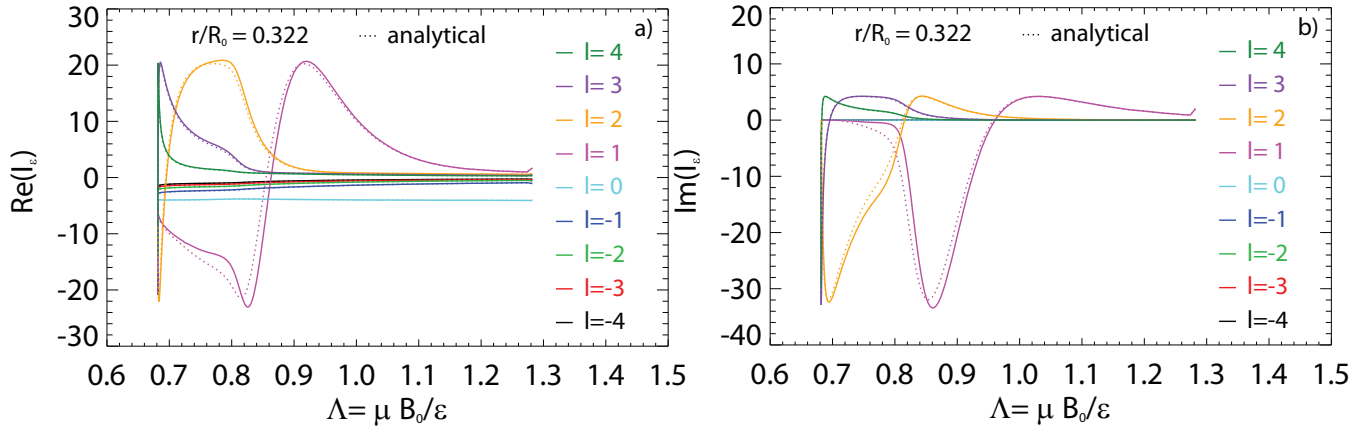

FIG. 12. a) Real and b) imaginary components of I_ε for each l from -4 to 4, vs. Λ for thermal ions in the ITER equilibrium at $r/R_0 = 0.322$ ($\Psi_n = 0.982$), calculated by `MISK`. Solid lines are the usual numerical method, while dashed lines use the analytical methods outlined in subsection V A.

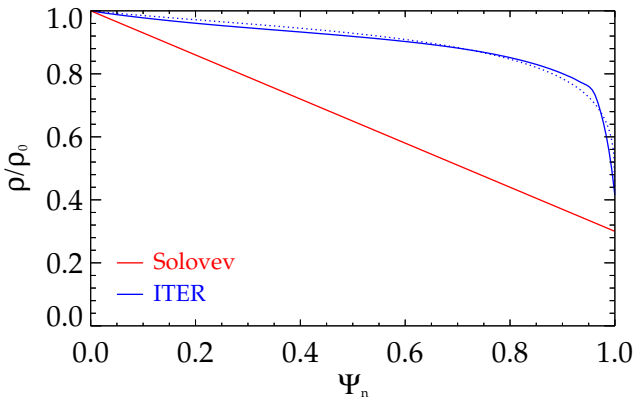

FIG. 13. Normalized mass density profiles for the Solov'ev and ITER cases. The dashed lines are the approximations used in PEST (nearly overlays in the Solov'ev case).

VI. EIGENFUNCTION COMPARISON

The normalized mass density profile, ρ/ρ_0, affects the eigenfunction. For the Solov'ev case, the normalized mass density profile $\rho/\rho_0 = (m_e n_e + m_i n_i + m_\alpha n_\alpha)/(m_e n_{e0} + m_i n_{i0} + m_\alpha n_{\alpha 0})$ reduces to $\rho/\rho_0 = 1 - 0.7\Psi_n$. For the ITER case ρ/ρ_0 is calculated from the individual density profiles and plotted in Fig. 13, along with the linear profile for the Solov'ev cases. PEST is limited in the mass density profiles it can take as an input, so approximations are used, which are shown in dashed lines.

Note that the PEST representation of ξ can be found in Ref. [19].

Figures 14a, 16a, and 18a compare the poloidal Fourier harmonics of the normal displacement $\xi \cdot \nabla\sqrt{\Psi_n}$ vs. $\sqrt{\Psi_n}$ for an ideal kink mode without a wall computed by MARS-K, MISHKA, and PEST for the Solov'ev 1, Solov'ev 3, and ITER cases, in PEST coordinates. The Fourier harmonics following this definition have more physical meaning (a better separation between resonant and non-resonant harmonics) than using equal-arc coordinates. The same quantity is plotted for the same equilibria in equal-arc coordinates in Figs. 14b, 16b, and 18b. Figure 16b can be directly compared to Fig. 10(a) of Ref. [13].

As an approximation to the fluid RWM, MISK uses the marginally stable ideal kink with an ideal wall, as calculated by PEST by moving the wall position progressively inward until the marginal point is found[2]. This eigenfunction is a good approximation to the fluid RWM[13]. Figures 15, 17, and 19 compare the poloidal Fourier harmonics of the normal displacement $\xi \cdot \nabla\sqrt{\Psi_n}$ vs. $\sqrt{\Psi_n}$ for a maginally stable ideal kink mode with an ideal wall computed by PEST to the fluid RWM eigenfunction computed by MARS-K, for the three equilibria in PEST coordinates and equal-arc coordinates. Since MISHKA does not include a resistive wall, it is not included in this comparison. Figure 17b can be directly compared to the fluid RWM eigenfunction in Fig. 10(b) of Ref. [13].

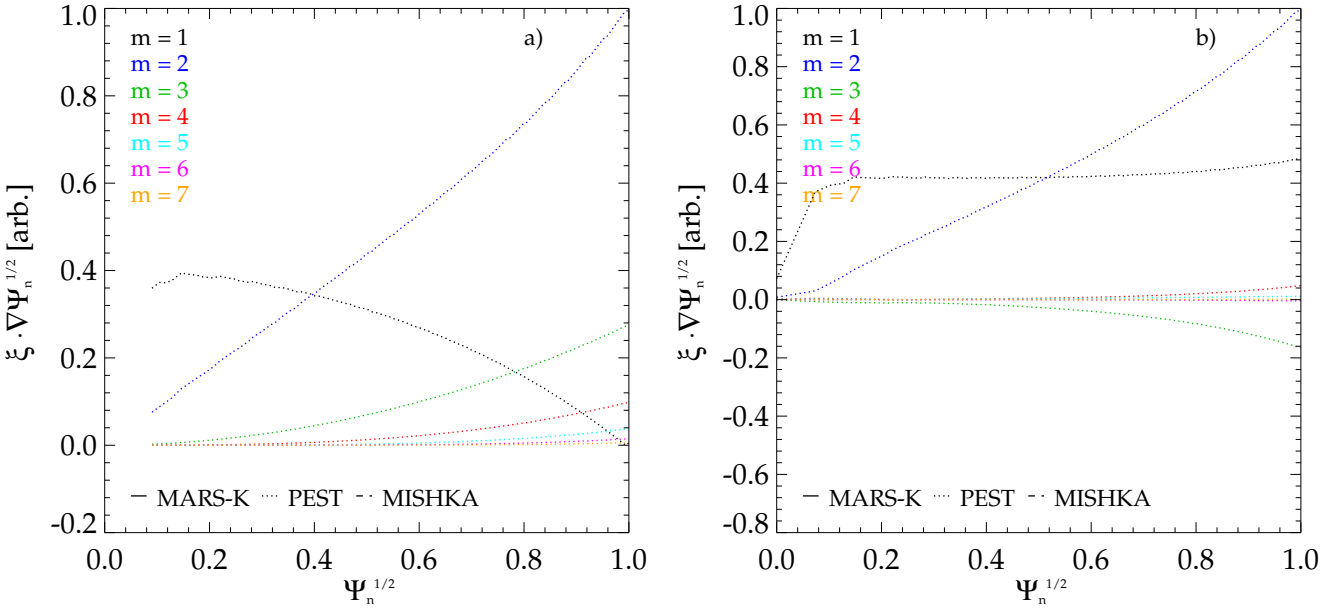

FIG. 14. Poloidal Fourier harmonics of the normal displacement for an ideal kink mode without a wall for the Solov'ev 3 equilibrium, as computed by MARS-K, MISHKA, and PEST, in a) PEST and b) equal-arc coordinate systems.

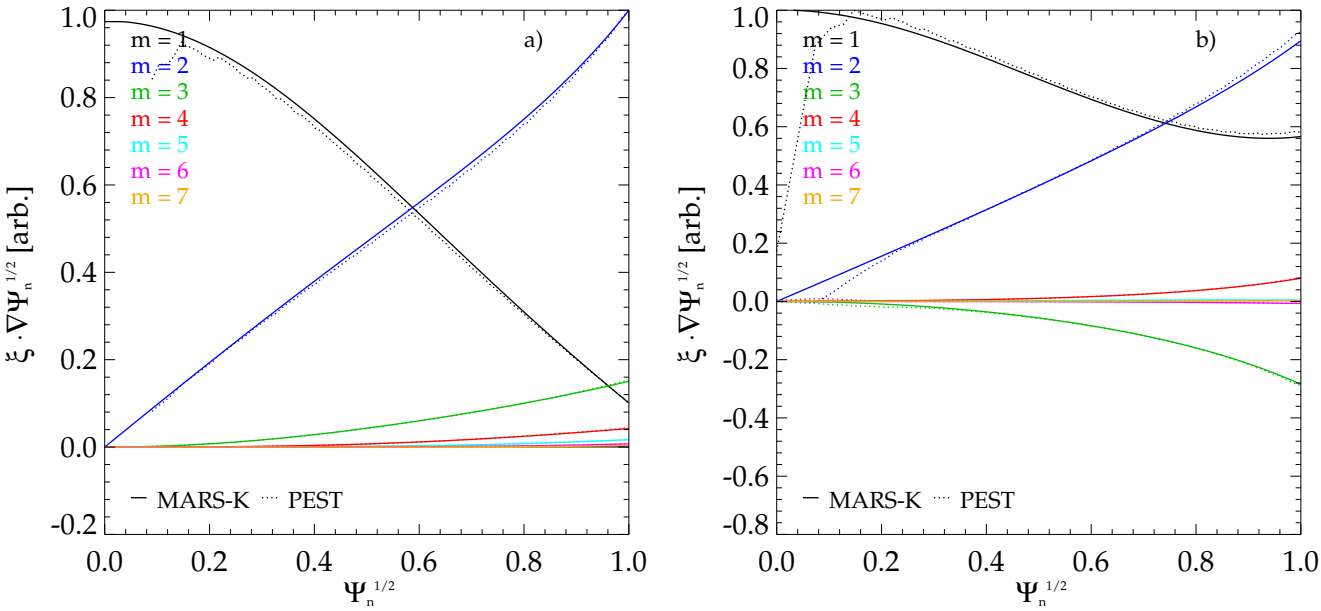

FIG. 15. Poloidal Fourier harmonics of the normal displacement for the marginally stable ideal kink mode with an ideal wall for the Solov'ev 1 equilibrium, as computed by PEST, and the fluid RWM eigenfunction as computed by MARS-K, in a) PEST and b) equal-arc coordinate systems.

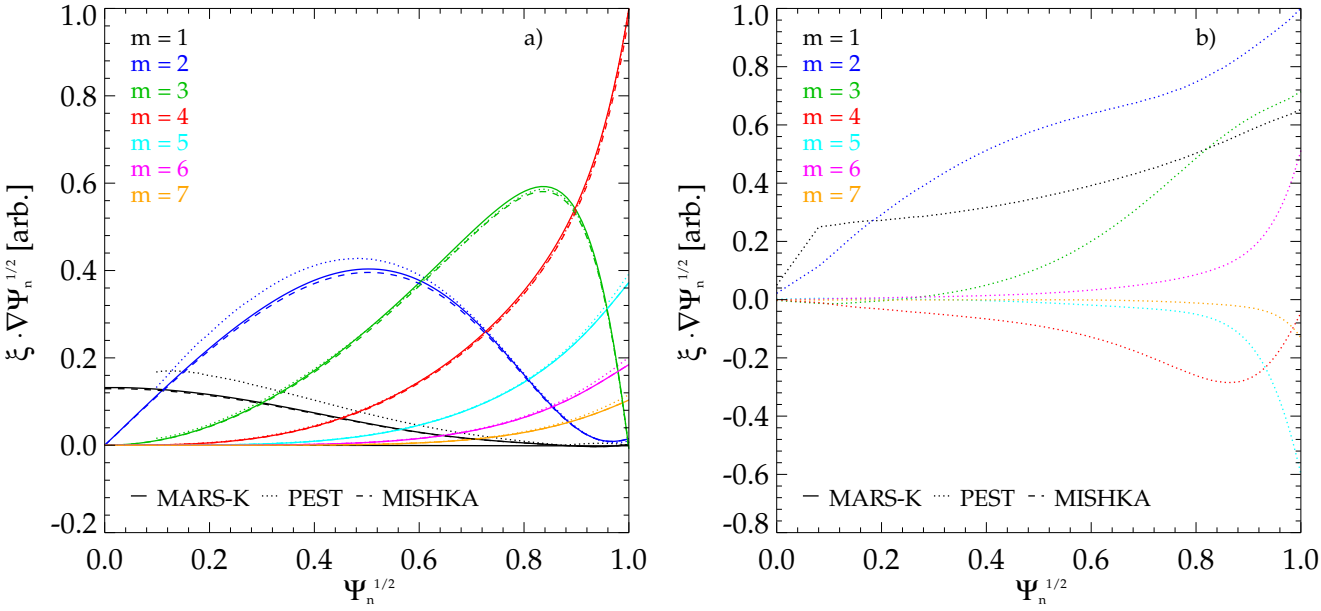

FIG. 16. Poloidal Fourier harmonics of the normal displacement for an ideal kink mode without a wall for the Solov'ev 3 equilibrium, as computed by MARS-K, MISHKA, and PEST, in a) PEST and b) equal-arc coordinate systems.

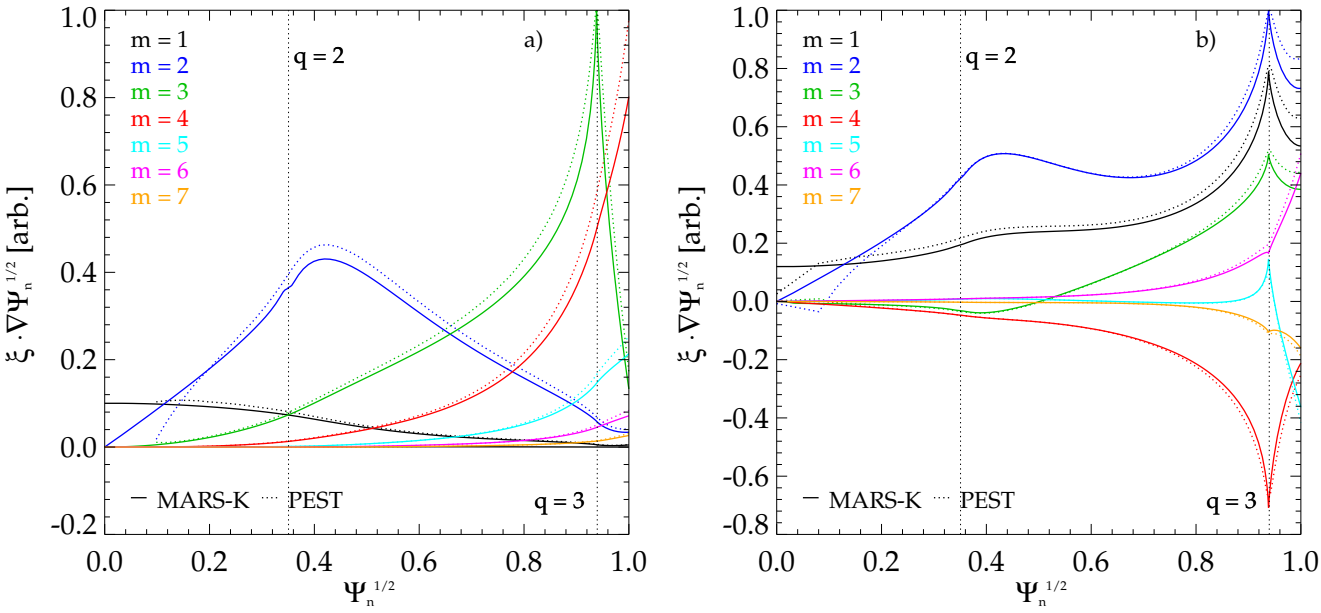

FIG. 17. Poloidal Fourier harmonics of the normal displacement for the marginally stable ideal kink mode with an ideal wall for the Solov'ev 3 equilibrium, as computed by PEST, and the fluid RWM eigenfunction as computed by MARS-K, in a) PEST and b) equal-arc coordinate systems.

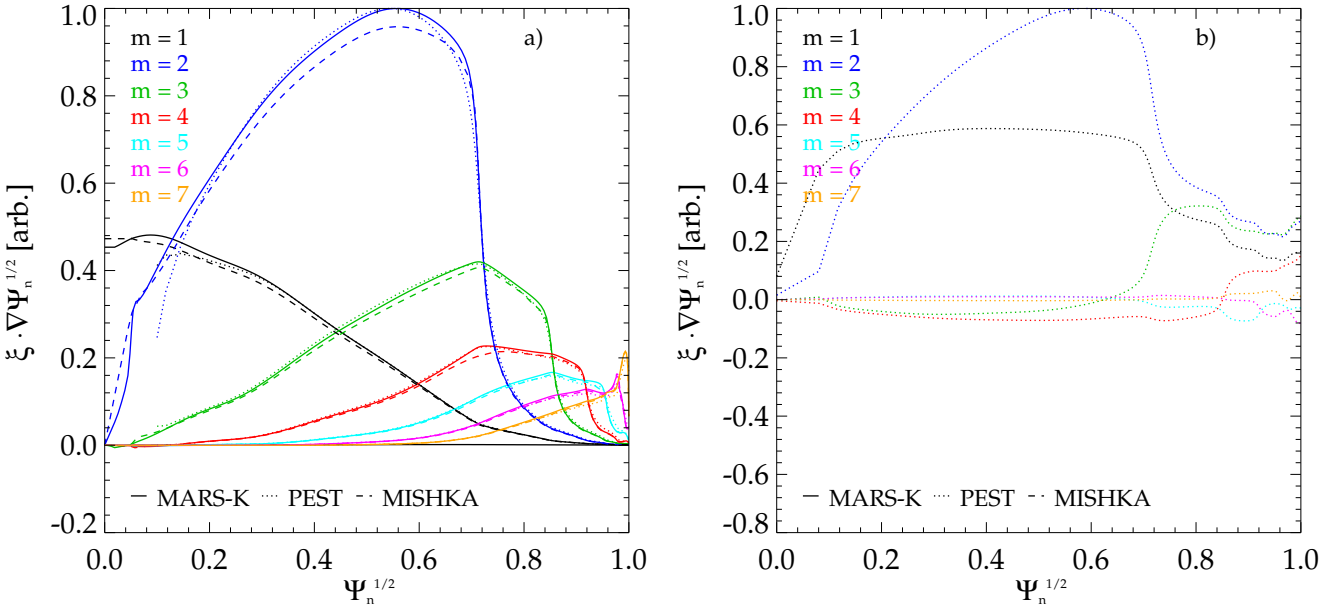

FIG. 18. Poloidal Fourier harmonics of the normal displacement for an ideal kink mode without a wall for the ITER equilibrium, as computed by MARS-K, MISHKA, and PEST, in a) PEST and b) equal-arc coordinate systems.

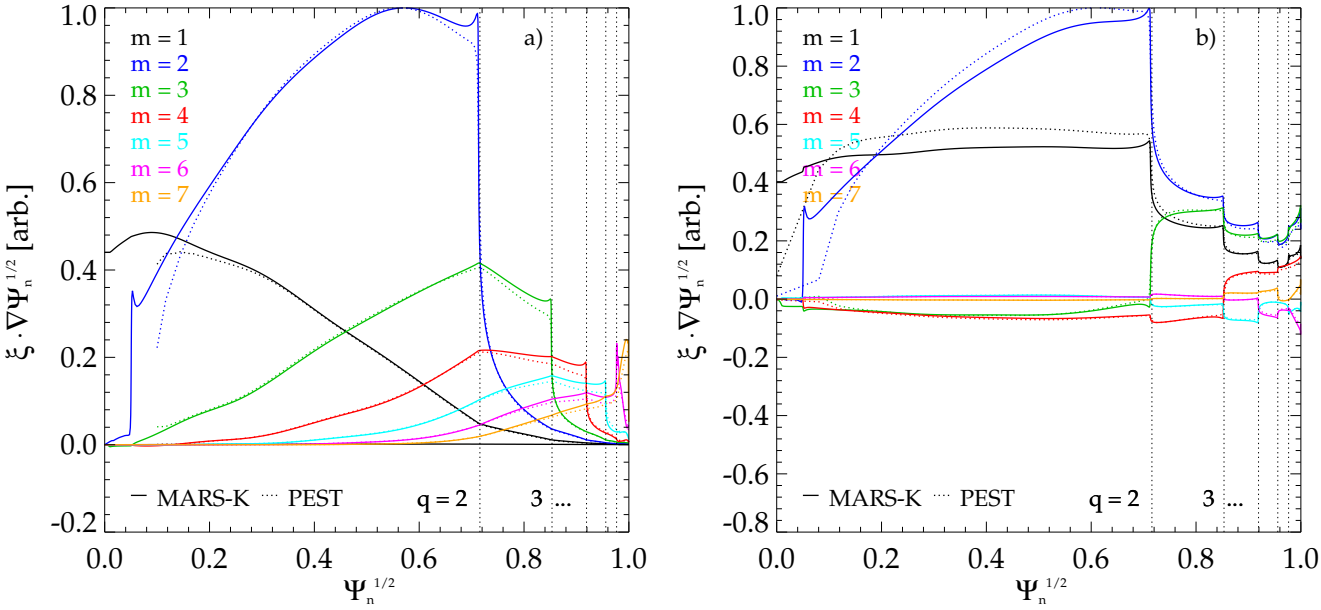

FIG. 19. Poloidal Fourier harmonics of the normal displacement for the marginally stable ideal kink mode with an ideal wall for the ITER equilibrium, as computed by PEST, and the fluid RWM eigenfunction as computed by MARS-K, in a) PEST and b) equal-arc coordinate systems.

VII. THE PERTURBED LAGRANGIAN

Another major part of the kinetic calculation is the perturbed Lagrangian, written here for trapped particles:

$$\langle H/\hat{\varepsilon}\rangle(\Psi,\Lambda,l)=\frac{1}{\tau}\oint\frac{1}{\sqrt{1-\frac{\Lambda B}{B_0}}}\left[\left(2-3\frac{\Lambda B}{B_0}\right)(\boldsymbol{\kappa}\cdot\boldsymbol{\xi}_\perp)-\left(\frac{\Lambda B}{B_0}\right)(\boldsymbol{\nabla}\cdot\boldsymbol{\xi}_\perp)\right]e^{-il\omega_b t}d\boldsymbol{\ell}. \tag{49}$$

Similarly to how the energy integral of the frequency resonance fraction can be calculated solely based on the frequencies and encompasses all the energy dependence of the problem, the perturbed Lagrangian can be calculated solely based on the eigenfunction, and indeed is the only place in the problem where the eigenfunction appears.

Like in section V with $I_{\hat{\varepsilon}}$, we can make plots of $\langle H/\hat{\varepsilon}\rangle$ vs. Λ for particular Ψ surfaces. Figure 20 shows each l component of $\langle H/\hat{\varepsilon}\rangle$ from -4 to 4 in the Solov'ev 1 equilibrium at $r/R_0=0.08$ ($\Psi_n=0.16$), the same surface chosen in Fig. 6. Figure 21 shows each l component of $\langle H/\hat{\varepsilon}\rangle$ from -4 to 4 in the Solov'ev 3 equilibrium at $r/R_0=0.252$ ($\Psi_n=0.585, q=2.5$).

Note that like the bounce and precession frequencies, this quantity has a singularity when $v_\parallel\to 0$, but it is integrable.

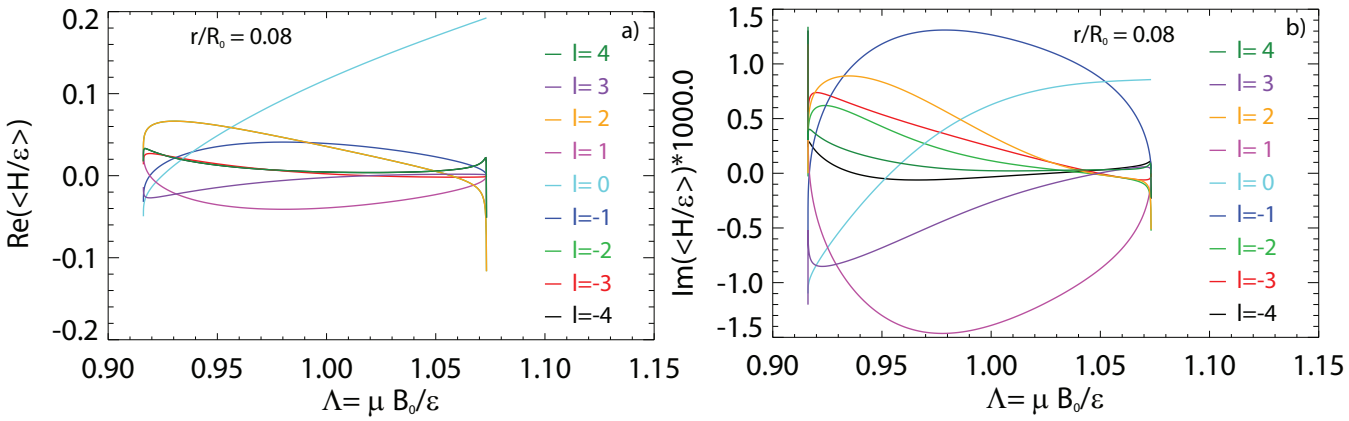

FIG. 20. a) Real and b) imaginary components of $\langle H/\hat{\varepsilon}\rangle$ for each l from -4 to 4, vs. Λ in the Solov'ev 1 equilibrium at $r/R_0 = 0.08$ ($\Psi_n = 0.16$), calculated by `MISK`.

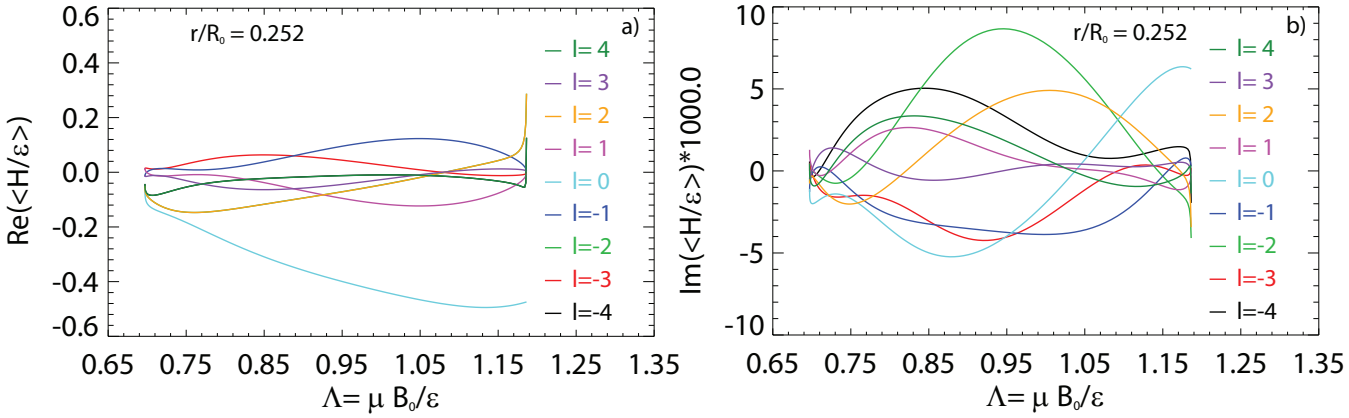

FIG. 21. a) Real and b) imaginary components of $\langle H/\hat{\varepsilon}\rangle$ for each l from -4 to 4, vs. Λ in the Solov'ev 3 equilibrium at $r/R_0 = 0.252$ ($\Psi_n = 0.585, q = 2.5$), calculated by `MISK`.

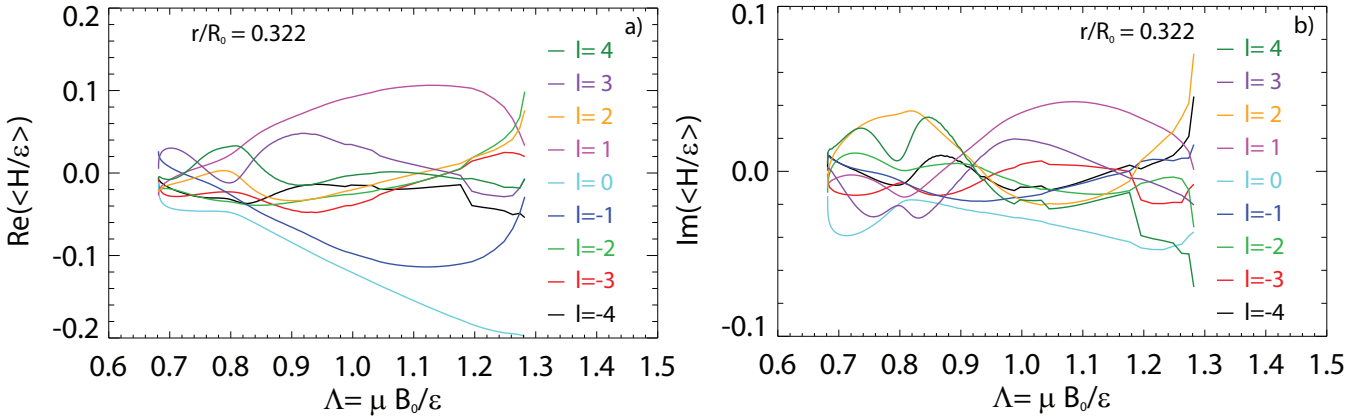

FIG. 22. a) Real and b) imaginary components of $\langle H/\hat{\varepsilon}\rangle$ for each l from -4 to 4, vs. Λ in the ITER equilibrium at $r/R_0 = 0.322$ ($\Psi_n = 0.982$), calculated by `MISK`.

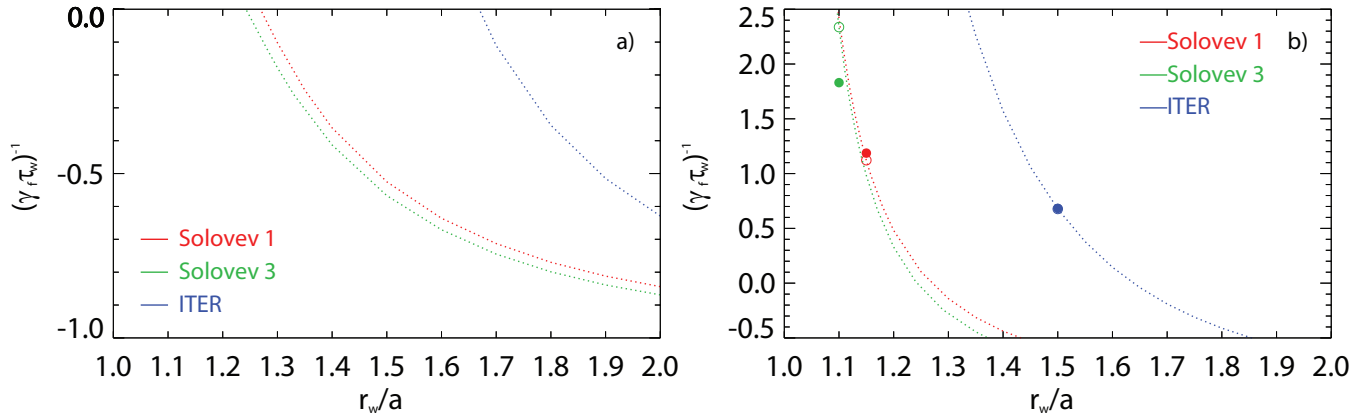

FIG. 23. The inverse fluid growth rate, normalized by the wall time, vs. normalized conformal wall position for the three cases for: a) the ideal kink, and b) the marginally stable ideal kink mode with an ideal wall (PEST) or the fluid RWM (MARS-K). PEST results are shown with dashed lines and open circles, MARS-K results with solid lines and solid circles. The circle markers shown in b) indicate the values at the wall positions chosen for comparison.

VIII. FLUID δW TERMS

δW_∞ and δW_b are the fluid terms calculated with the wall at infinity or the actual "experimental" location b. In this study we will use a conformal wall, so that b is the distance of the wall away from the plasma boundary, in units of r/a, and the normalized wall position is $r_w/a = 1 + b$. The absolute value of these δW quantities as calculated by different codes is arbitrary. What really matters are the ratios. Therefore in this section we will report the quantity

$$\hat{\gamma}_f^{-1} = -\frac{\delta W_b}{\delta W_\infty}, \tag{50}$$

which is the inverse fluid growth rate, normalized by the wall time.

Let us now also define $\delta W_\infty = \delta W_F + \delta W_S + \delta W_V^\infty$, the sum of the plasma fluid, surface, and vacuum perturbed potential energies when the wall is placed at infinity (the no-wall condition), and $\delta W_b = \delta W_F + \delta W_S + \delta W_V^b$, the sum of the plasma fluid, surface, and vacuum δW terms when the wall is placed at a specific location b. The PEST code uses the VACUUM code[20] to calculate the δW_V terms. The plasma fluid terms are equal regardless of the wall position. The surface term arises when there is a finite pressure gradient at the plasma boundary. This term is not calculated by MARS or PEST.

Once δW_∞ is found, δW_b, and therefore $\hat{\gamma}_f^{-1}$ can be examined as a function of r_w/a. This is shown for the three cases in Fig. 23a for the ideal kink mode and can be directly compared to Ref. [13], Fig. 3, for the Solov'ev 1 case. Here we will instead use the eigenfunction for the marginally stable ideal kink mode with an ideal wall in PEST (approximating the fluid RWM) and the fluid RWM in MARS-K. Figure 23b shows $\hat{\gamma}_f^{-1}$ vs. r_w/a for these cases.

For the Solov'ev 1 case we will choose $r_w/a = 1.15$, and for Solov'ev 3 $r_w/a = 1.10$, to be consistent with Ref. [13], even though the value of $\hat{\gamma}_f^{-1}$ will be different than used in that work. See Fig. 1 for illustrations of these conformal walls. For the ITER case, we choose both a conformal wall with $r_w/a = 1.5$, or the actual ITER wall. See Fig. 3 for illustrations of these walls. In PEST the wall position is chosen as the second inner-most black line in Fig. 3, which is the center of the thick inner wall.

In PEST the fluid δW quantities have a dependency on the selection of $\Psi_{\rm lim}$. For the Solov'ev cases $\Psi_{\rm lim} = 1$ can be used, but for the ITER case here we have used $\Psi_{\rm lim} = 0.9976$, which results in $q_{\rm edge} = 6.96168$.

The results are given in Table III.

IX. KINETIC δW_K

For trapped Maxwellian particles, the kinetic δW is given by

	r_w/a	$\delta W_F/(-\delta W_\infty)$	$\delta W_V^b/(-\delta W_\infty)$	$\hat{\gamma}_f^{-1} = \delta W_b/(-\delta W_\infty)$
Solov'ev 1	1.15	-1.814 -1.793	3.001 2.915	1.187 1.122
Solov'ev 3	1.10	-2.257 -2.210	4.087 4.547	1.830 2.337
ITER	1.50	-6.284	6.966	0.682 0.677
	actual			1.664

TABLE III. `MARS-K` results are red, `PEST` results are blue. Note that $\delta W_S = 0$, so $\delta W_V^\infty/(-\delta W_\infty)$ can be inferred from $1 + \delta W_F/(-\delta W_\infty)$.

$$\delta W_K = -\frac{\sqrt{\pi}}{2}\int_0^{\Psi_a}\frac{nT}{B_0}\int_{B_0/B_{\max}}^{B_0/B_{\min}}\tau\sum_l|\langle H/\hat{\varepsilon}\rangle|^2 I_{\hat{\varepsilon}}\,d\Lambda d\Psi. \tag{51}$$

One can see that the energy integral involves the previously defined quantities $I_{\hat{\varepsilon}}$ and $\langle H/\hat{\varepsilon}\rangle$ in a straightforward way.

Once again, the absolute value of δW_K is meaningless, so we will report the values found as $-\delta W_K/\delta W_\infty$, broken into its various contributions in table IV.

For the Solov'ev 1 case, with all the nominal frequency profiles from section IV, `MISK` finds quite small values of $-Re(\delta W_K)/\delta W_\infty = 0.0243$ and $-Im(\delta W_K)/\delta W_\infty = 0.0280$. There are no energetic particles for this case, and no rational surfaces, so there is no Alvén layer contribution.

	thermal ions						thermal electrons		Alfvén Layer		Total	
	trapped				circulating		trapped ($l=0$ only)					
	$l=0$		$l\neq 0$									
	real	imag	real	imag	real	imag	real	imag	real	imag	real	imag
Solov'ev 1	8.46×10^{-2}	-1.48×10^{-2}	3.10×10^{-3}	-5.11×10^{-5}	-2.10×10^{-3}	-1.33×10^{-4}	-6.00×10^{-2}	2.95×10^{-3}			2.56×10^{-2}	-1.21×10^{-2}
	1.45×10^{-2}	2.23×10^{-6}	3.84×10^{-3}	8.12×10^{-3}	-8.90×10^{-3}	2.05×10^{-2}	1.58×10^{-2}	3.68×10^{-5}	0	0	2.51×10^{-2}	2.87×10^{-2}
Solov'ev 3											2.08×10^{-1}	-3.43×10^{-1}
	1.90×10^{-1}	2.50×10^{-6}	-8.69×10^{-3}	1.45×10^{-2}	4.03×10^{-3}	3.93×10^{-2}	1.90×10^{-1}	6.46×10^{-5}	-3.81×10^{-5}	-1.20×10^{-5}	3.71×10^{-1}	1.46×10^{-2}
ITER												
	8.52×10^{-1}	3.05×10^{-4}	-9.96×10^{-2}	2.68×10^{-2}	-2.23×10^{-1}	3.78×10^{-2}	1.35×10^{-1}	-1.64×10^{-2}	-1.03×10^{-2}	-7.95×10^{-1}	6.53×10^{-1}	-7.46×10^{-1}

TABLE IV. $\delta W_K/(-\delta W_\infty)$. `MARS-K` results are red, `MISK` results are blue.

A. The Kruskal-Oberman Limit

The results for the Kruskal-Oberman limit described in subsection V A 1 are given in Table V. In this case circulating electrons and trapped electrons with a bounce ($l \neq 0$) resonance become important, so they are included as well.

	thermal ions			thermal electrons			Total
	trapped		circulating	trapped		circulating	
	$l = 0$	$l \neq 0$		$l = 0$	$l \neq 0$		
Solov'ev 1	1.11×10^{-2}	1.02×10^{-2}	9.69×10^{-2}	1.11×10^{-2}	1.02×10^{-2}	9.69×10^{-2}	1.57×10^{-1} 2.36×10^{-1}
Solov'ev 3	1.16×10^{-1}	4.84×10^{-2}	1.80×10^{-1}	1.16×10^{-1}	4.84×10^{-2}	1.80×10^{-1}	6.89×10^{-1}
ITER	5.83×10^{-1}	5.20×10^{-1}	2.74	7.02×10^{-1}	6.01×10^{-1}	3.30	8.46

TABLE V. $\delta W_K/(-\delta W_\infty)$ in the Kruskal-Oberman limit ($|\omega_E - \omega| \to \infty$). `MARS-K` results are red, `MISK` results are blue. All values are real, and the total doe snot include the Alfvén layer contribution.

B. MISK Numerical vs. Analytic Energy Integral Results

`MISK` can now be run with the energy integral being calculated numerical, as usual, or analytically for trapped thermal ions and electrons, according to the formulae in Sec. V A. The results for the zero damping case are given in table VII. The real parts are equal, while the imaginary parts are different. This may be indicative of the fact that the analytical approach takes into account poles on the real axis, which the numerical approach does not. However, we have found that the resulting residues are only a part of the difference. This difference goes away when damping is increased (finite γ).

	thermal ions				thermal electrons			
	trapped				trapped			
	$l = 0$		$l \neq 0$		$l = 0$		$l \neq 0$	
	real	imag	real	imag	real	imag	real	imag
Solov'ev 1	1.45×10^{-2} 1.45×10^{-2}	2.23×10^{-6} 4.47×10^{-6}	3.84×10^{-3} 4.40×10^{-3}	8.12×10^{-3} 8.34×10^{-3}	1.58×10^{-2} 1.58×10^{-2}	3.68×10^{-5} 7.38×10^{-5}	-7.67×10^{-6} -8.01×01^{-6}	2.11×10^{-8} 5.07×10^{-10}
Solov'ev 3	1.90×10^{-1} 1.90×10^{-1}	2.50×10^{-6} 4.88×10^{-6}	-8.69×10^{-3} -8.30×10^{-3}	1.45×10^{-2} 1.56×10^{-2}	1.90×10^{-1} 1.90×10^{-1}	6.46×10^{-5} 1.27×10^{-4}	-7.55×10^{-6} -7.94×10^{-6}	4.79×10^{-8} 4.36×10^{-11}
ITER	8.52×10^{-1} 8.52×10^{-1}	3.05×10^{-4} 6.11×10^{-4}	-9.96×10^{-2} -1.04×10^{-1}	2.68×10^{-2} 3.56×10^{-2}	1.35×10^{-1} 1.35×10^{-1}	-1.64×10^{-2} -3.30×10^{-2}	-2.65×10^{-5} -4.34×10^{-5}	-1.11×10^{-5} -2.97×10^{-6}

TABLE VI. $\delta W_K/(-\delta W_\infty)$. `MISK` numerical (usual) results are blue, `MISK` analytic results are in black. This is for the case of no damping ($\nu_{\text{eff}} = 0$, and $\gamma = 0$.

C. Convergence vs. Damping Parameter

A damping parameter in the denominator of the resonance operator can come either from the finite growth rate of the RWM (γ), or from collisonality (ν_{eff}). δW_K should converge to the same value as that of the "ideal" case without any damping, when these damping terms approach zero. Figure 24 shows the results of such a convergence study for the Solov'ev 1 case.

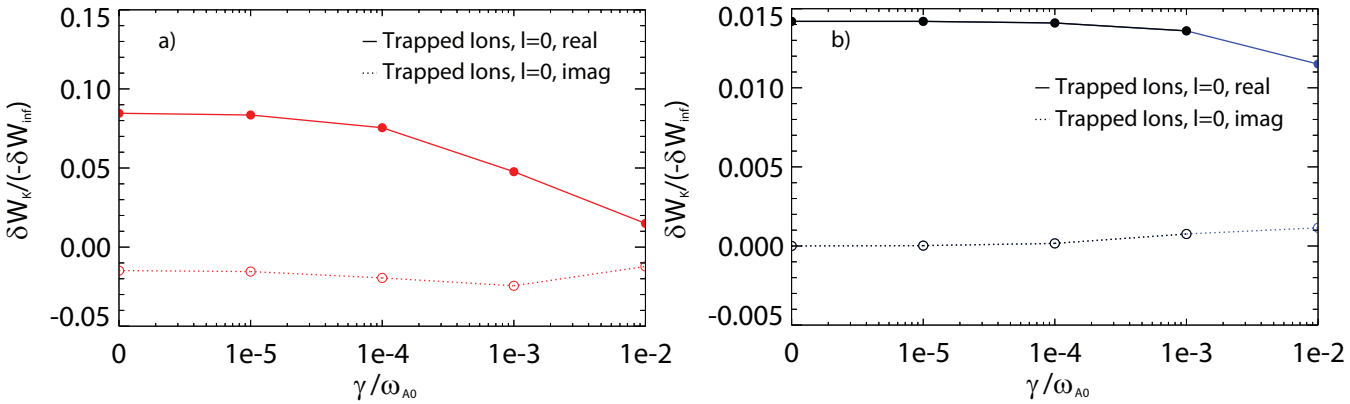

FIG. 24. Convergence of δW_K versus damping for the Solov'ev 1 case, as calculated by a) MARS-K, and b) MISK. For MISK, blue indicates numerical evaluation of the energy integral and black indicates analytical.

X. GROWTH RATE AND MODE ROTATION FREQUENCY

The RWM dispersion relation can be written[2,13,21]:

$$(\gamma - i\omega_r)\tau_w = -\frac{\delta W_\infty + \delta W_K}{\delta W_b + \delta W_K}. \tag{52}$$

The change in potential energy due to kinetic effects, δW_K, in general has both real and imaginary parts. The real part of ω is the mode rotation frequency, and is given by:

$$\omega_r \tau_w = \frac{Im(\delta W_K)(\delta W_b - \delta W_\infty)}{(\delta W_b + Re(\delta W_K))^2 + (Im(\delta W_K))^2}, \tag{53}$$

and solving for the imaginary part, we find the normalized growth rate:

$$\gamma\tau_w = -\frac{\delta W_\infty \delta W_b + (Im(\delta W_K))^2 + (Re(\delta W_K))(\delta W_\infty + \delta W_b + Re(\delta W_K))}{(\delta W_b + Re(\delta W_K))^2 + (Im(\delta W_K))^2}. \tag{54}$$

For the Solov'ev 1 case, with the nominal frequency profiles, MISK finds that the growth rate is barely changed from the fluid case. This is consistent with the previous analysis in Ref. [13], although, again, the cases are different because of the different eigenfunction used, as well as the different ω_E profile.

The results are given in table VII.

	r_w/a	$\gamma\tau_w$	$\omega\tau_w$
Solov'ev 1	1.15	8.04×10^{-1} 8.49×10^{-1}	-1.80×10^{-2} -4.62×10^{-2}
Solov'ev 3	1.10	3.50×10^{-1} 2.32×10^{-1}	-2.28×10^{-1} -6.65×10^{-3}
ITER	1.50	-4.12×10^{-2}	5.38×10^{-1}
	actual		

TABLE VII. MARS-K results are red, MISK results are blue.

ACKNOWLEDGMENTS

The authors would like to thank...

This research was supported by the U.S. Department of Energy under grants DE-FG02-99ER54524 (Columbia University) and ...

[1] R. Grimm, J. Greene, and J. Johnson, "Methods in computational physics, vol. 16," Chap. Computation of the Magnetohydrodynamic Spectrum in Axisymmetric Toroidal Confinement Systems.
[2] B. Hu, R. Betti, and J. Manickam, Physics of Plasmas **12**, 057301 (2005).
[3] B. Hu, R. Betti, and J. Manickam, Physics of Plasmas **13**, 112505 (2006).
[4] J. W. Berkery, S. A. Sabbagh, R. Betti, B. Hu, R. E. Bell, S. P. Gerhardt, J. Manickam, and K. Tritz, Physical Review Letters **104**, 035003 (2010).
[5] J. W. Berkery, S. A. Sabbagh, H. Reimerdes, R. Betti, B. Hu, R. E. Bell, S. P. Gerhardt, J. Manickam, and M. Podesta, Physics of Plasmas **17**, 082504 (2010).
[6] S. A. Sabbagh, J. W. Berkery, R. E. Bell, J. M. Bialek, S. P. Gerhardt, J. E. Menard, R. Betti, D. A. Gates, B. Hu, O. N. Katsuro-Hopkins, B. P. LeBlanc, F. M. Levinton, J. Manickam, K. Tritz, and H. Yuh, Nuclear Fusion **50**, 025020 (2010).
[7] J. W. Berkery, S. A. Sabbagh, R. Betti, R. E. Bell, S. P. Gerhardt, B. P. LeBlanc, and H. Yuh, Physical Review Letters **106**, 075004 (2011).
[8] Y. S. Park, S. A. Sabbagh, J. W. Berkery, J. M. Bialek, Y. M. Jeon, S. H. Hahn, N. Eidietis, T. E. Evans, S. W. Yoon, J. Ahn, J. Kim, H. L. Yang, K. I. You, Y. S. Bae, J. Chung, M. Kwon, Y. K. Oh, W. Kim, J. Y. Kim, S. G. Lee, H. K. Park, H. Reimerdes, J. Leuer, and M. Walker, Nuclear Fusion **51**, 053001 (2011).
[9] H. Reimerdes, J. W. Berkery, M. J. Lanctot, A. M. Garofalo, J. M. Hanson, Y. In, M. Okabayashi, S. A. Sabbagh, and E. J. Strait, Physical Review Letters **106**, 215002 (2011).
[10] J. W. Berkery, R. Betti, and S. A. Sabbagh, Physics of Plasmas **18**, 072501 (2011).
[11] L. Solov'ev, Zh. Eksp. Teor. Fiz. **53**, 626 (1967).
[12] M. S. Chance, J. M. Greene, R. C. Grimm, J. L. Johnson, J. Manickam, W. Kerner, D. Berger, L. C. Bernard, R. Gruber, and F. Troyon, Journal of Computational Physics **28**, 1 (1978).
[13] Y. Liu, M. S. Chu, I. T. Chapman, and T. C. Hender, Physics of Plasmas **15**, 112503 (2008).
[14] F. Villone, Y. Liu, G. Rubinacci, and S. Ventre, Nuclear Fusion **50**, 125011 (2010).
[15] A. Bondeson and M. S. Chu, Physics of Plasmas **3**, 3013 (1996).
[16] Y. Liu, M. S. Chu, C. G. Gimblett, and R. J. Hastie, Physics of Plasmas **15**, 092505 (2008).
[17] M. Rosenbluth and M. Sloan, Physics of Fluids **14**, 1725 (1971).
[18] M. D. Kruskal and C. R. Oberman, The Physics of Fluids **1**, 275 (1958).
[19] S. Preische, J. Manickam, and J. Johnson, Computer Physics Communications **76**, 318 (1993).
[20] M. Chance, Physics of Plasmas **4**, 2161 (1997).
[21] B. Hu and R. Betti, Physical Review Letters **93**, 105002 (2004).